This is a repository copy of *Manipulating the water–air interface to drive protein assembly for functional silk-like fibroin fibre production*.

White Rose Research Online URL for this paper:
https://eprints.whiterose.ac.uk/221268/

Version: Published Version

Article:

Manipulating the water–air interface to drive protein assembly for functional silk-like fibroin fibre production

Check for updates

Rafael O. Moreno-Tortolero [1,2] ✉, Juliusz Michalski[1], Eleanor Wells[1], Flora Gibb[1], Nick Skaer[3], Robert Walker[3], Louise Serpell [4], Chris Holland [5] & Sean A. Davis [1] ✉

Silk's remarkable properties arise from its hierarchical structure, formed through natural transformation from an aqueous solution to a solid fibre driven by pH and flow stress under low-energy conditions. In contrast, artificial silk fabrication typically relies on extrusion-based methods using coagulating baths and unnatural solvents, limiting true biomimetic replication. Here, we find that native-like silk fibroin forms viscoelastic films at the air-water interface. Utilizing this, we demonstrate a mild, all-aqueous method to seamlessly pull silk-like fibres with co-aligned nanofibrillar bundles. The fiber structure transitioned from hexagonally packed β-solenoid units at low pulling speeds to β-sheet-rich structures at higher speeds. Fibers pulled near physiological speeds (26.3 mm s^{-1}) exhibited optimal mechanical properties, with an elastic modulus of 8 ± 1 GPa and toughness of 8 ± 5 MJ m^{-3}, comparable to natural silk. This platform also enables embedding nanoparticles and biologics, offering broad applications in sensors, biocatalysis, and tissue engineering, expanding the potential of silk-based composite materials.

Silk fibroin has captivated researchers for generations owing to its remarkable mechanical properties and unique self-assembly behavior[1]. As a result, this natural process has proven inspirational for the production of a whole host of silk-like fibres from synthetic components[2,3]. However, unlike synthetic materials, silk fibroin undergoes a, not fully understood, programmed transition from a liquid aqueous solution to a solid state with minimal energy input, making it a fascinating subject of study[4,5].

Recent investigations have provided further insight into the molecular self-assembly mechanism of *Lepidoptera* silk fibroin, revealing its nanofibrillar structure in the Silk-I configuration and the intricate interactions driving its solidification[6]. At the macroscopic level, natural silk fibres are not extruded but rather pulled into shape through a process akin to pultrusion[7,8]. This pultrusive mechanism, observed in silkworms and spiders, underpins the biomechanical sophistication of silk production in nature[9].

Reconstituted silk fibroin (RSF), although often used as a precursor in biomimetic silk materials research, has some inherent limitations due to its reduced molecular weight and the lack of the N-terminal domain (NTD) responsible for pH-controlled supramolecular assembly[10]. As a result, RSF requires non-native conditions, such as organic solvents[11], coagulation baths[12], or prepolymerised aggregates[13], for fibre formation[14,15]. However,

these methods impose environmental stress on the protein and deviate from the natural spinning process where only minimal energy inputs are required to fabricate the silk fibre[7,13,16].

Interestingly, both silk fibroin and spidroins exhibit surface-active properties, rapidly forming elastic films at the water–air interface[17,18]. Although the surface activity of native or native-like fibroin remains underexplored, recent insights into the protein's structural dynamics suggest that the water–air interface plays a crucial role in directing assembly in-vitro[19]. By leveraging this behaviour, our aim was to fabricate silk-like fibres with enhanced control and efficiency.

In this study, we propose a novel approach to silk fibre fabrication that harnesses the interfacial self-assembly of silk fibroin and its sensitivity to stresses. The method was developed from observations made while working with dilute native-like silk fibroin (NLSF) solution (see ST 1 and Figures S1, S2). Notably, we overcame some key processing issues related to using native and native-like silk fibroin precursor solutions to produce fibrous materials. Concentrated fibroin solutions are highly shear sensitive[20,21], and this property severely inhibits any attempt to mix and disperse dopants or combine with other phases. We circumvent this problem by using dilute solutions of the protein which tends to then

[1]School of Chemistry, University of Bristol, Cantock's Close, Bristol, UK. [2]Max Planck-Bristol Centre for Minimal Biology, School of Chemistry, University of Bristol, Bristol, UK. [3]Orthox Ltd; Milton Park, 66 Innovation Drive, Milton, Abingdon, UK. [4]Sussex Neuroscience, School of Life Sciences, University of Sussex; Falmer, Brighton, UK. [5]School of Chemical, Materials and Biological Engineering, University of Sheffield, Mappin Street, Sheffield, UK. ✉e-mail: ro.morenotortolero@bristol.ac.uk; s.a.davis@bristol.ac.uk

concentrate at the water–air interface. Moreover, additional dispersants can be easily introduced into the aqueous subphase and subsequently, readily incorporated into the resulting silk-fibre. This very mild approach, that takes advantage of the natural assembly properties of the protein, offers considerable benefits when producing living composites The use of low protein concentrations, and the absence of coagulating baths and organic solvents altogether offers an environment amenable to introducing living cell components, that would otherwise suffer from osmotic shocks (when using concentrated protein stocks or salt baths) or be exposed to toxic organic solvents (like hexafluoro isopropanol, a common solvent for silk and silk-like protein)[22].

In brief, fibroin molecules adsorb at the water–air interface and by applying perpendicular extension we induce a strain field. Pulling the film in this way promotes the more ordered alignment and registration of solenoid units via lateral interactions and subsequent consolidation leads to fibre formation. Our proposed molecular level mechanism is illustrated in Fig. 1 (Video 1). We believe this method offers a promising alternative to conventional methods, allowing to produce silk-like fibres under more physiologically relevant conditions. Although similar observations have also been reported for recombinant spidroin systems[23,24], these have not recognised the role of the interface in driving assembly, nor more importantly have shown evidence of scalability of the process.

Overall, our study seeks to deepen our understanding of silk fibroin assembly and pave the way for the development of biomimetic materials with tailored properties and applications. By bridging the gap between fundamental research and practical applications, we aim to unlock the full potential of silk fibroin as a versatile biomaterial.

Results and discussion

### Interfacial assembly of the protein at the water–air interface

To better understand our initial observations and validate our proposed process, the surface assembly properties of the protein were studied. Although it is known that concentration plays a role in the interfacial properties of the protein, given the high complexity of the system and for simplicity, this work only used a single concentration, ca. 6 mg/mL and studied the effect of pH on the protein assembly at the water–air interface. This concentration was determined empirically as offering a suitable balance between film interface stability, monomer replenishment via diffusion, and bulk viscosity to facilitate fibre pulling.

In the first instance, we determined the adsorption behaviour of the protein at the water–air interface, and the effect of pH. To do this, interfacial surface tension (IFT) analysis was done using a Wilhelmy plate. In this experiment, the force that a platinum plate is subjected to when wetted with
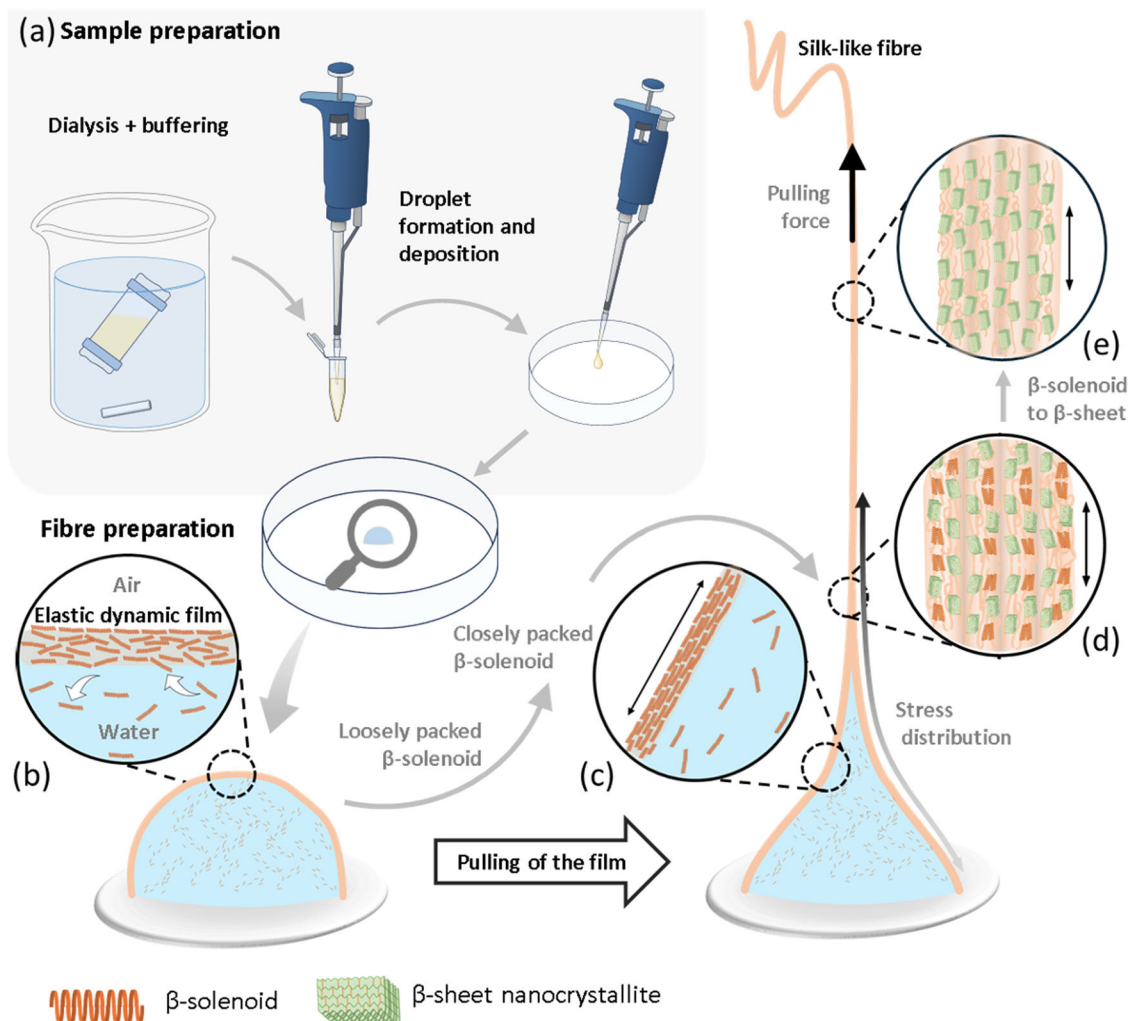
Fig. 1 | Proposed process, assembly and fabrication of the biomimetic pulled silk-like fibre. Briefly, NLSF protein at 2 wt% in 8.5 M LiBr is dialyzed against Milli-Q water, then buffered and stored in plastic tubes at 4 °C until use. For fabrication, the protein solution is gently pipetted, and 50–100 μL are deposited as droplets onto clean plastic petri dishes (**a**). A continuous filament is then pulled directly from the film that forms at the water–air interface. This interfacial film is believed to consist of a network of loosely packed β-solenoids (**b**). As the film is pulled, the elongated proteins are forced to align and pack more closely together (**c**). Once a critical stress is applied, the proteins within the filament undergo further denaturation (**d**), forming β-sheet nanocrystallites (**e**).
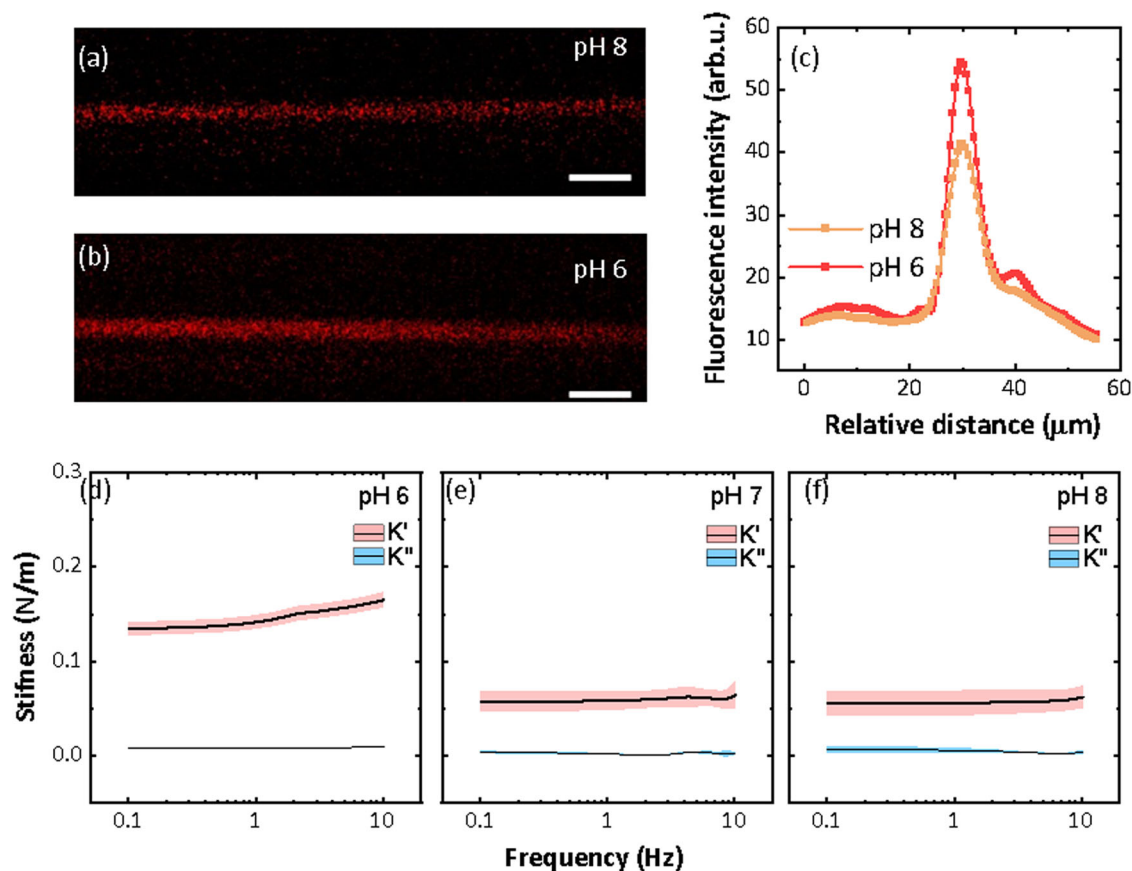
Fig. 2 | Confocal Laser Scanning Microscopy (CLSM) analysis of the self-assembled silk fibroin film at the water/air interface. X-Z projection of the film formed from solution buffered at pH 8 (**a**) and 6 (**b**). Fluorescence intensity 1D profile across the interface shows estimated films' thickness at pH 8 and 6 (**c**). Dynamic micro-indentation of the protein film formed at pH 6, 7 and 8 showing elastic (red) and viscous (blue) components of stiffness plotted as stiffness against frequency (**d–f**, respectively). Scale bars (**a**) and (**b**) are 20 μm.

a liquid is related to surface tension by Eq. 1:

$$\gamma = \frac{F}{L \cos \theta} \quad (1)$$

Where γ is the interfacial surface tension, L is the length of the plate, and θ is the wetting angle. The advantage of this system is that it allows for the measurement of adsorption kinetics on long timescales without suffering as much from evaporative effects. Inspired by the natural pH gradient within the insect and our own observations, only pH values of 8, 7 and 6 were used, as any lower pH tended to promote rapid aggregation at the concentration tested. Figure S3 shows the results from these experiments. In all cases, very rapid adsorption was observed, with all experiments showing a reduction in IFT even at the beginning of the experiment. Despite samples at pH 6 and 7 behaving similarly, the protein absorbs to the interface much quicker at high pH, with an apparent lower IFT value. Notably, the observed values agree with RSF values observed at similar concentrations[18].

To some extent, these experiments verify previous observations[10], where silk proteins displayed smaller hydrodynamic diameters, hence, faster diffusion rates at higher pH. This indicates that the protein at pH 8 has a faster adsorption to the interface due to faster diffusion speeds under these conditions. Still, the difference in the value of IFT itself is more nuanced. It is possible to argue that there might be changes in the total accessible surface area of the protein, whereby at pH 8, the protein exists as a monomeric unit, with a higher likelihood of forming a different type of oligomeric units as pH is decreased. Oligomerisation or aggregation would then reduce the total accessibly surface area of the protein. Because the concentration was constant, such reduction in the IFT could be described by Equation S1[25]. Further

discussion and observations can be found in ST 2, describing more in depth observations of a solid-to-solid transformation driven by stress, see Video 2 and Figures S4, S5.

To characterise the morphology of the protein film at the water–air interface, we used confocal laser fluorescence microscopy (CLFM). Here, intrinsic fluorescence was used with no labelling, to avoid changes in the assembly behaviour by incorporating fluorescent labels, which commonly react with free primary amines or carboxylate groups (i.e. Lys or Asp/Glu residues) which are only present at the terminal domains or linker units[6]. This is particularly relevant given the important role NTD has on driving assembly[26,27]. In these experiments, about 10 μL of solution equilibrated at either pH 8, or 6 was placed in individual wells and left to age for about 5 h before observing the air/water interface using a long-working distance objective (x10). Results are shown in Fig. 2a, b. Despite the films being of similar thickness (10–20 μm, as seen in Fig. 2c), the relative fluorescence intensity of the protein at pH 6 is higher, which could indicate an aggregation-induced emission (AIE) process[28]. Freely rotating Tyr (mainly) might be now locked in a single rotameric state, enhancing the fluorescence of these multimers/aggregates against the protein in solution. These observations would support our hypothesis of a higher degree of order/oligomerisation at lower pH. However, a high degree of order is also imparted by the geometrical restriction of the interface itself and the elongated nature of the protein, producing a significant signal at higher pH. Further insights into this process could be gained by studying the thickness evolution of the protein film as it is being pulled during fibre formation and is subject of ongoing research.

In order to characterise the mechanics of the films, they were subjected to dynamic micro-indentation measurements. A small indenter was placed
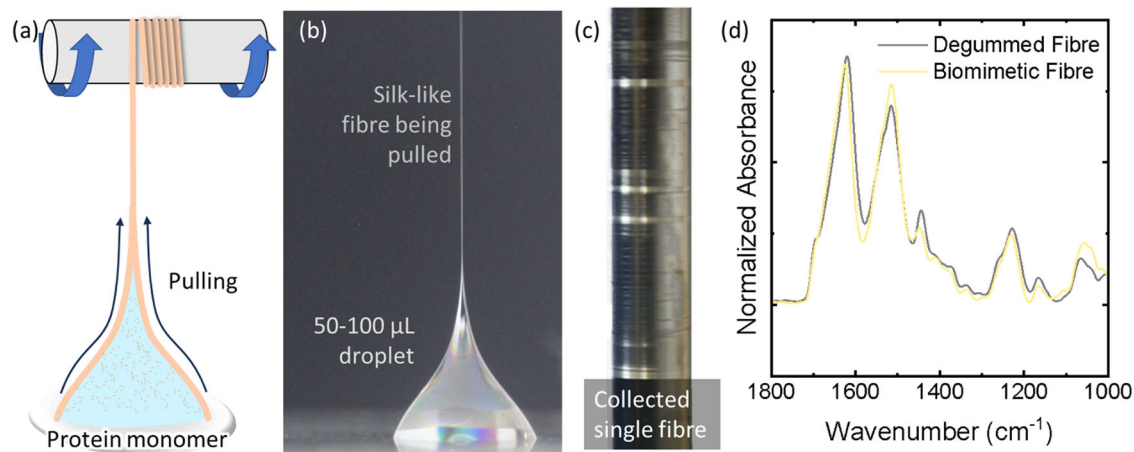
Fig. 3 | Fabrication of single fibres extending several metres in length and their characterization using FTIR analysis. Schematic representation of the general setup for fibre fabrication, with a rotating mandrel collecting the fibre as it is being pulled from the interfacial film (**a**), a photograph of the droplet as it is being pulled gently

(**b**), example of a 5 m long fibre collected onto stainless steel mandrel (**c**) and FTIR analysis of natural degummed fibroin fibre and biomimetic fibre produced at 15.6 mm/s of the protein fingerprint region (1800 – 100 cm−1) (**d**).

in contact with the film and later oscillated, with small oscillation amplitudes, at a range of frequencies (0.1 – 10 Hz). Using this method, we determined the viscoelastic response in terms of the separate elastic and viscous components of the same. The results are shown in Fig. 2d–f. In these experiments, the measurements are reported as Stiffness (K) against frequency, with stiffness calculated as the measured force divided by the indentation depth, or half the oscillation amplitude. K' and K" will refer to the elastic and viscous components, respectively. Much as expected, the material at pH 6 showed a relatively higher K' (160 ± 1 mN m^{-1}) value than its counterparts at pH 7 or 8 (60 ± 2 and 60 ± 3 mN m^{-1}, respectively), which showed little difference between them. At lower pH, the nature of the protein in solution is likely oligomeric, driven by the NTD interactions; hence the effective MW of the system is increased, increasing the total cohesiveness, which is translated to a higher modulus. This supported previous observations made by us that NLSF undergoes a switch-like behaviour occurring at pH just below 7[10].

Biomimetic silk-like fibre fabrication and characterisation
Taken together, these observations indicate that there is an elastic, yet dynamic film formed very rapidly at the water/air interface. However, despite the rapid assembly at the water/air interface, we have only been able to pull fibres from small droplets with a volume of up to 100 µL, and not from larger volumes, indicating that there is an interplay between protein assembly, and other physical parameters of the droplet, such as curvature that are currently under investigation.

We report that upon extensional strain/stress applied by pulling, it is possible to assemble insoluble silk-like fibres. For simplicity and knowing that the film was more resilient at pH 6, this condition was used and exploited to produce single fibres many meters long by continuously pulling using the method depicted in Video 3 and summarised in Fig. 3a. Simply by depositing small droplets onto standard plastic petri dishes it was possible to pull fibres at different speeds. The achieved pulling speeds were from 1.8 mm/s up to about 53 mm/s; although the fibre formation was less stable at higher speeds. We hypothesise that this is due to a competition between the film formation and the depletion of protein by the formation of the fibre. However, the covered range contains the natural silkworm spinning speeds estimated to be between 10 and 30 mm/s[29].

Using this method, with droplets of between 50 and 100 µL (Fig. 3b), it was possible to produce single fibres up to 10 m in length (Fig. 3c). All fibres presented a highly hierarchical morphology, with the main fibre formed by bundles of sub-micron fibres composed of smaller nanofibrils as seen in Figure S2. The results obtained by SEM corroborate these observations and are summarised in Fig. 4a–f. The fibrillar network is extended far away from

the place where the mature fibre emerges as outlined in Fig. 4a, with the experimental observations shown in Fig. 4b. We were also able to observe individual nanofibrils, without much evidence of branching. In other words, the smaller observable fibrils seem to be growing in one dimension and only interacting by relatively weaker lateral interactions to form the larger bundles. These observations not only are in line with the current understanding of the natural silk fibre[30], and the process of consolidation recently observed by Wan et al. [21,31], it would also be predicted from our proposed fibre assembly model; Tyr residues limit the lateral docking of strands, much like the lateral docking of β-solenoids, making the nanofibrillar interface, yet facilitate other type of interactions such as π-π or methyl-π. It has been observed that native silk fibroin fibres can be exfoliated into increasingly thinner fibrils, ranging from 20−100 nm bundles, down to 3.1 ± 0.8 nm and ultimately into an extended chain with a diameter of about 3.7 ± 0.9 Å[30]. We observed significant variation in the apparent nanofibril diameter with the pulling speed (Fig. S6). The largest nanofibril diameters of 184 ± 18 and 219 ± 47 nm corresponded to the highest pulling speeds studied of 32.2 and 52.7 mm/s respectively. A minimum in nanofibril diameter of 52 ± 6 nm was observed at a pulling speed of 10.7 mm/s. For all other pulling speeds (1.8, 5.9, 15.9, 21, 26.3 mm/s) the nanofibril diameters were relatively constant in the range 71 ± 14 nm to 84 ± 10 nm.

In the interest of understanding the biological relevance of our method in the context of in-vivo fibre production, we measured the forces that were required to pull these fibres[7]. At steady-state. We measured a force of about 0.45 ± 0.04 mN at a pulling speed of 15.5 mm s^{-1}, well within the forces that the insect can exert[32,33]. No significant difference in the forces were observed at different speeds (Figure S7a), indicating that by varying the pulling speeds we were more likely changing the strain rate, and not the stress overall. Further chemical analysis of the fibres, beyond the nanoscopic similarity with natural silk fibres, showed a remarkable resemblance of the molecular structure, with the amide-I peak showing similar nominal β-sheet, β-turn and statistical coil composition (see Fig. 4d). Thus, indicating a transformation from soluble silk fibroin (silk-I) to the well-known insoluble conformation (silk-II) by just using pH control and mechanical stimulation. Although small differences were observed in the deconvoluted fold contributions from the FTIR spectra of the different produced fibres, these very small differences are difficult to interpret, given that β-solenoid vibrational contributions are less characterised and tend to overlap with contributions from disordered regions (see Figure S8)[34,35].

To further understand the effect of pulling speeds at the molecular level, we conducted fibre X-ray diffraction (fXRD) experiments on the different fibres immediately after being produced at different pulling speeds. In silk fibres, it is known that the protein takes an extended chain
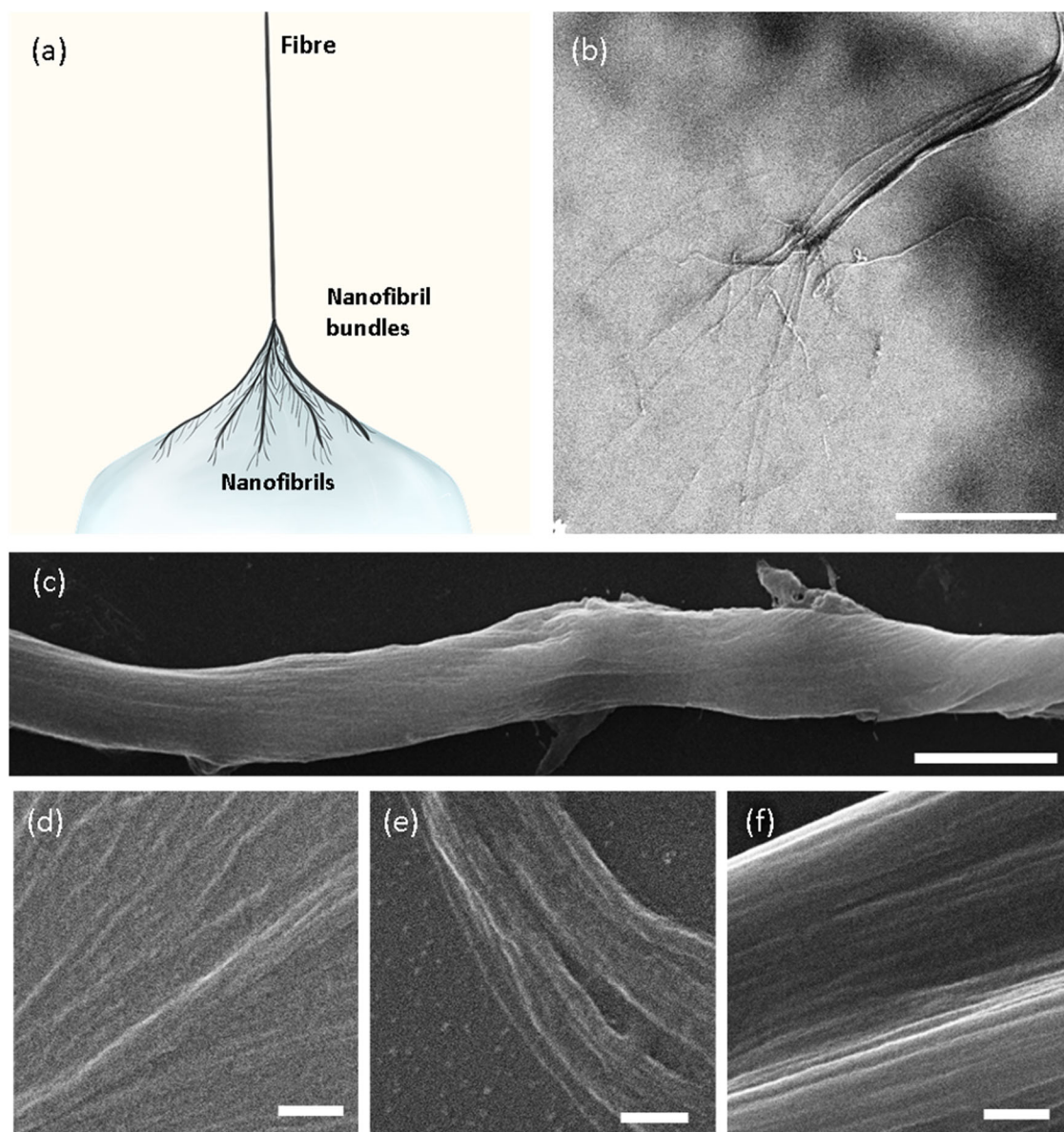
Fig. 4 | Structural characterisation of the hierarchical silk-like fibres produced by pulling protein films from the water–air interface. Drawing representing the hierarchical organisation of the fibres, from the moment of fabrication at the water–air interface of a droplet (**a**) SEM micrograph of fibre pulled and dried on mica (**b**) SEM micrograph of a different fibre at higher magnification showing evidence of striated texture indicative of microfibrillar internal structure (**c**) SEM micrograph of the same fibre showing detail in another area of nanofibrils (**d**), nanofibril bundles joining (**e**), and closer details of the bundle (**f**). Scale bars are 100 μm in (**b**). 5 μm in image (**c, e**), 1 μm in (F) and 500 nm in image (**d**).

conformation, wherein the hydrogen bond network is perpendicular to the long axis of the fibre. However, this conformation is drastically different from our Silk-I model, a β-solenoid structure. In the proposed fibre formation process, the solenoids would be aligned parallel to the water/air interface plane, and upon drawing, these would align with the long axis of the created filament. The solenoids are denatured/stretched upon applying critical strain rate and stress, and the known Silk-II configuration emerges.

Hence, here we would expect to observe at least a two regime effect, where at low stresses a dominating Silk-I structure is obtained, while at higher stresses a dominating and aligned Silk-II structure is favoured, similarly as predicted before[36]. Indeed, this was observed going from a pulling speed of about 1.8 mm s^{-1} to about the maximum possible of approximately 52.7 mm s^{-1}. This is demonstrated in Fig. 5a, where there is a reflection corresponding to about 17 Å at the lowest pulling speeds, which disappears as pulling speed increases. We interpret this reflection as coming from a hexagonal packing of hydrated solenoid units (Figure S9), which

upon reaching a critical strain rate are disrupted, prompting extension of the backbone and collapse of the chains in β-sheets. This transition is captured by the strengthening of the reflections associated to β-pleated sheets, in particular the increased intensity of the off-meridian 3.85 Å at higher pulling speeds, consistent with the prediction in our previous work[10]. It is important to note that no pure β-solenoid fibre was isolated from our experiments, which is in line with the known sensitivity of this structure to mechanical stimulation[37], and might explain the small differences observed by FTIR.

Following these experiments, we conducted single fibre tensile testing (Fig. 5b, c). Figure 5b shows the averaged stress-strain curves obtained for the fibres produced at different pulling speeds, already showing noticeable differences. Figure 5c compares key derived physical properties (elastic modulus, tensile strength, strain at break, toughness and diameter) of the biomimetic fibres with each other and with native, degummed fibroin fibres. More detailed data and statistics are found in Figure S9. While our fibres exhibit lower mechanical properties compared to natural fibroin,
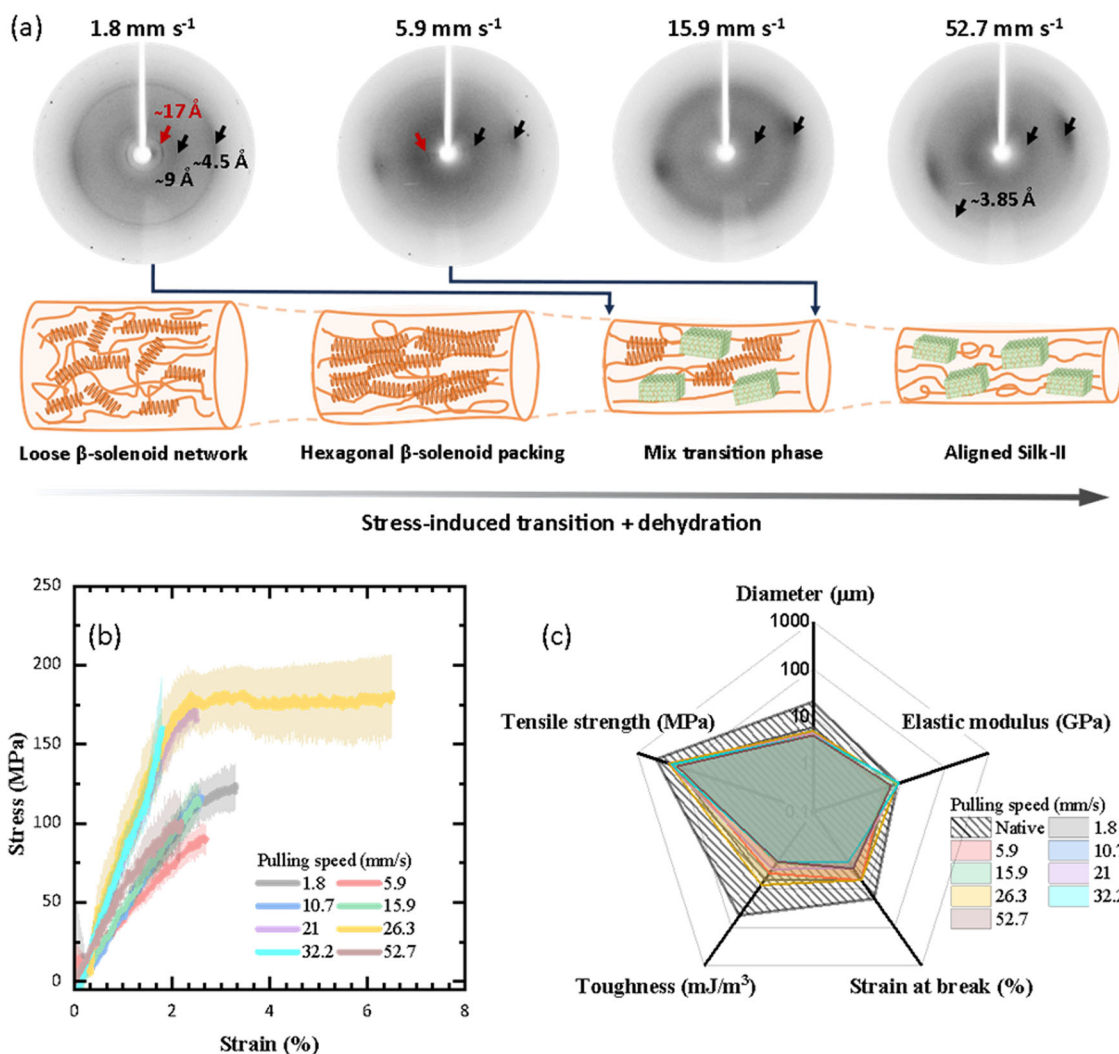
Fig. 5 | Fibre XRD patterns and mechanical properties obtained for different fibres formed under various pulling speeds. Red arrow indicates the reflection assigned to the hexagonal packing of the solenoid units (ca. 16 Å) and black arrows indicate typical Silk-II reflections (ca. 9.5, 4.5 and 3.85 Å) accompanied by schematic cartoon representing the proposed transition from loosely packed β-solenoid units, to hexagonally packed and further denatured to collapse in β-sheet nanocrystallites that make up most the matured silk fibre (**a**). Average single fibre tensile testing for fibres produced at different pulling speeds (**b**), and polar plot comparing native silkworm fibroin fibre key determined properties elastic modulus diameter, tensile strength, strain at break and toughness against the fabricated fibres (**c**).

particularly in extensibility and toughness, it is important to note that all properties are within the same order of magnitude. We anticipate further improvement if the testing geometry is adjusted (e.g., reducing the overall length of the specimens) and additional post-processing methods are applied[13,38].

We observed improved mechanical properties at pulling speeds corresponding to the fastest natural spinning speeds (ca. 30 mm/s), with the mechanical properties decreasing thereafter. Briefly, Elastic modulus showed no significant differences from the lowest pulling speed of 1.8 mm s^{-1} up to 15.9 mm s^{-1}, with the values ranging between 4–5 GPa, however, from 21 to 32.2 mm s^{-1} we observed increased modulus, between 8 and 10 GPa, decreasing back to 6 ± 1 GPa for the fastest pulling speed (52.7 mm s^{-1}), see Figure S10a. The values of tensile strength followed a similar trend, with strength increasing for the pulling speeds between 21 and 26.3 mm s^{-1} to almost 200 MPa for these, and decreasing monotonically as the pulling speed increased thereafter, see Figure S10b.

Interestingly, a slightly different trend was followed by the maximum strain and toughness values, where these showed a second maxima at the minimal pulling speed (1.8 mm s^{-1}). The maximum extensibility was found to be about 6% for both 1.8 and 5.9 mm s^{-1}, falling to about 3% for the pulling speeds from 10.7 to 21 mm s^{-1}, after which extensibility increased again to

6 ± 4% for the fibres produced at 26 mm s^{-1}, only to fall back to about 3% for any of the faster pulling speeds, see Figure S10c. Similarly, the same trend was observed for toughness, see Figure S10d.

Interestingly, the observed trends are different from the fibre diameter trends, which only showed a monotonic decrease going from 6 ± 1 μm to 3.7 ± 0.2 μm, for fibres produced at 1.8 and 52.7 mm s^{-1}, respectively (see Figure S7b), indicating a decoupling of the tensile properties from fibre diameter most likely as a result of a change in the hierarchical structure within the fibre. Moreover, the overall results are readily explained by our fXRD data, together with the observation of the variability in diameter of the nanofibrils, indeed support our model, where we predict the existence of multiple regimes that depend on stress and stress rate.

At the lowest pulling speeds, the relatively higher content of Silk-I conformation would enable a higher extensibility (and toughness), without necessarily enhancing other properties such as elastic modulus or tensile strength, as the lower strain rates would also imply a lower orientation of the formed β-sheet crystallites. On the other hand, the observation of the overall properties showing a maximum at the peak of natural spinning speeds might indicate the formation of an optimal protein network architecture, where the balance of crystallite size, distribution and orientation maximises the properties of the material, in particular its toughness. Although our
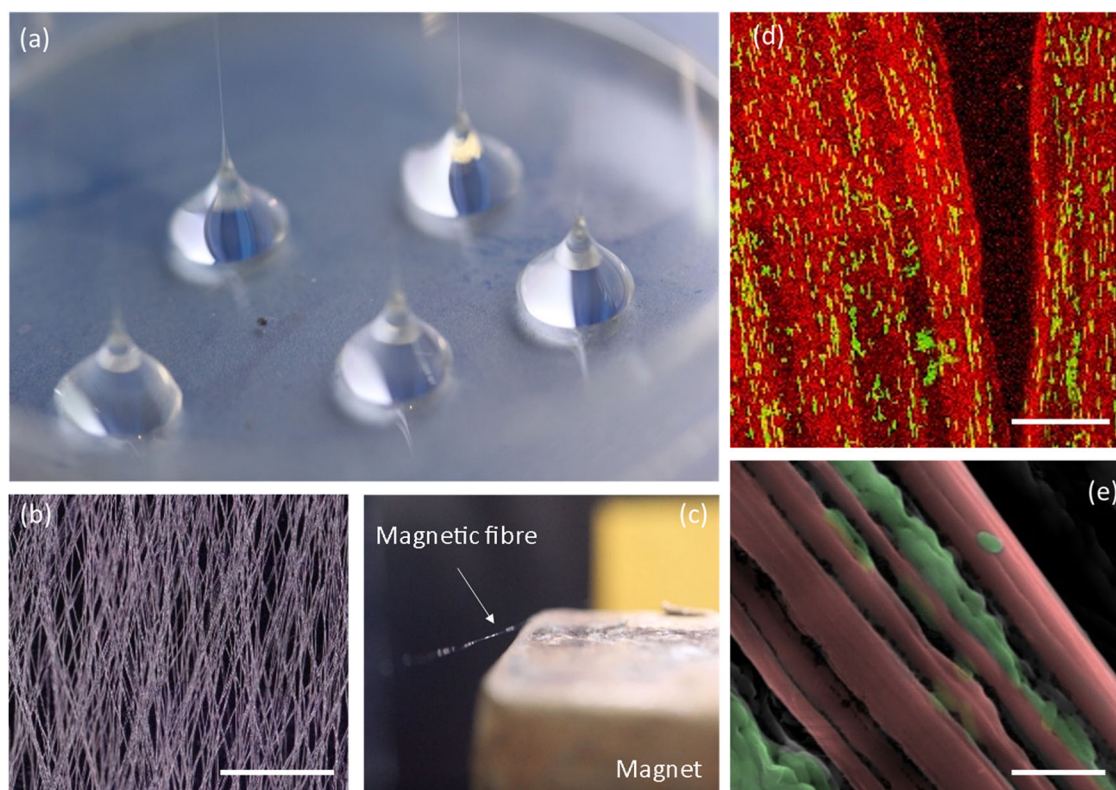
Fig. 6 | Exploiting the droplet-pulling method for the fabrication of advanced fibrous materials. Photograph of several droplets of NLSF being simultaneously pulled (**a**). Photograph of a fabricated non-woven multi-ply mat (**b**). Photograph of a silk-like fibre composite with magnetite nanoparticles interacting with a neodymium magnet (**c**). Maximum intensity projection along Z-stacks obtained via confocal fluorescence of a *E. coli*/silk-like fibre composite with bacteria producing GFP in green and silk protein intrinsic fluorescence in red (**d**). Colour enhanced SEM image of the *E. coli*-silk-like fibre composite, showing integrated *E. coli* cells (green) within the nanofibrillar bundles (red) (**e**); scale bars are 1 mm (**b**), 50 μm (**d**) and 4 μm (**e**).

system might not fully recapitulate the in-vivo system, mainly due to the concentration differences, it is notable that here we observe an optimum at the natural spinning speeds.

Our proposed fibre formation mechanism involves two separate steps; first the oligomerisation of NTD driven by pH reduction, and later the reconfiguration of the network and further denaturation of the protein fold driven by stress. In this sense, the oligomerisation of NTD effectively reduces the degrees of freedom of the protein while also breaking the symmetry of the system. This first step endows orientation, registration and fosters network formation, priming the protein for the second step: stress driven assembly.

The fabrication approach we propose here recapitulates this two-step process, first by breaking the symmetry of the system by exposing it to a interface, inherently asymmetric, and further driving the assembly by stress. Here, in purely aqueous solutions, without any precipitants (salts or solvents) and by using high-quality protein feedstock we were able to replicate the Silk-I to Silk-II transformation, using relative speeds and forces that are accessible to the animal.

Besides the fundamental implications of our observations, the presented method represents a facile, biomimetic process that allows for the easy and efficient fabrication of silk-like fibres. Its simplicity is amenable for the fabrication of several composite materials. For example, multiple fibres can be pulled simultaneously (Fig. 6a) while moving the platform along the collector/mandrel to fabricate non-woven mats (see Video 4 and Figure S11 explaining the principle). Using standard ideas for the fabrication of non-woven fibrous mats of about 2 × 4 cm were manufactured only using about 500 μL of the protein solution (Figure S11b).

Moreover, due to the low viscosity of the bulk feedstock, the process allows for facile bottom-up incorporation of functionality into the produced fibres. In the past, functional silk fibres have been formed by either modifying the surface chemistry of the natural fibres[39], or directly feeding the insect with functional particles[40]. Here, by simply dispersing functional particles into the low viscosity protein solution, we were able to fabricate magnetic silk-like fibres with incorporated magnetite nanoparticles (Fig. 6c and Figure S12).

However, we believe that our system offers significant advantages to produce hybrid, living materials. To demonstrate this, we chose *Escherichia coli* (*E. coli*), transformed with an Isopropyl β-d-1-thiogalactopyranoside (IPTG) inducible Green fluorescent protein (GFP) containing plasmid, as an exemplar biocomponent as it is used extensively in biotechnological applications[41]. Significantly we show our processing is compatible with encapsulating cells and that *E. coli* retains its metabolic activity. Despite the relatively large size of *E. coli*, these were readily and homogeneously incorporated (Fig. 6d, e), with strong evidence of preferential alignment of the elongated bacteria in the same direction of the fibrils (Video 5), as directional analysis of the images shows in Figure S13. We believe the orientation is induced mainly due to the confinement offered by the hierarchical nanofibrillar morphology of the fibres, and not necessarily by the flow, as the forces used here are low. We are continuing our research to further optimize our platform and extend the scope to other fibrous composite materials and device manufacture.

Conclusions

In this work we present a novel methodology to produce silk-like fibres that recapitulates many of the natural steps and requires minimal energy input. The process exploits the rapid formation of a protein film at the water–air interface, which upon stretching, undergoes orientation and fibrillation. Although we only present results with NLSF, the process can likely be generalised to other surface-active, rheologically "sticky" proteins and polymers. Furthermore, these results reinforce our recently proposed self-

assembly pathway where pH and shear promote fibre formation from a protein that belongs to the β-solenoid family. The applied stress/strain not only aligns the fibrillar protein, but upon a critical stress/strain rate, promotes unfolding and extension of the protein backbone, allowing for extensive β-sheet formation.

Using this simple process, multiple meter-long silk-like fibres were produced that showed native-like mechanical properties without further need of post-treatment. Moreover, the simplicity and versatility of this mild method allows for the facile bottom-up fabrication of a myriad of fibrous composites, demonstrated here by incorporating both magnetite nanoparticles and GFP transformed *E. coli*. Although the method is limited in the throughput as compared to electrospinning, it offers a cost-effective, minimal energy and mild method, amenable for the fabrication of biohybrid fibrous composites. Overall, with this work we present a novel material fabrication method, which has the potential be expanded beyond silk and offers unprecedented insight in the assembly mechanism of silkworm fibroin into macroscopic fibres.

Materials and Methods

Native-like silk fibroin solution (NL-SF)
Fibroin solutions of 8.5 M LiBr and 20 wt% of protein were kindly provided by Orthox LTD in 60 mL syringes and stored at 4 °C until used. Briefly, silk fibres were initially treated as per patent number US 8,128,984B2 using mild degumming conditions to minimize fibroin hydrolysis, after washing with MilliQ water, fibres were gently dried and dissolved in 8.5 M LiBr at 60 °C over 4 h. A stock solution at 2 wt% was made for studies requiring diluted solutions by diluting the provided solution with 8.3 M LiBr. The 20 wt% solutions look clear, free of precipitates, with a distinctive pale-yellow tint and low-shear viscosity of 60 ± 3 Pa.s. The stock solutions were then dialysed against MilliQ water using $12-14$ kDa molecular weight cut-off dialysis membranes, with regular water changes to fresh MilliQ water changes. LiBr removal was followed by conductivity measurements of the dialysate and contrasted against a conductivity calibration curve, often requiring 3–4 days of dialysis to remove 99.9% of LiBr salt. After dialysis the 2 wt% yields a clear liquid solution with viscosity like pure water, and concentrations in the range of 5–7 mg/mL. Concentrations were determined gravimetrically by aliquoting about 500 μL of the solution and lyophilising them overnight in a Labconco Freezone 2.5 L Freeze-drier.

Fourier-Transform Infrared Spectroscopy (FTIR)
Fibres were analyzed directly using a Perkin Elmer Spectrum One FTIR spectrometer with an Attenuated Total Reflectance (ATR) accessory equipped with a diamond window and the supplemented Spectrum analyzer software. The analyzed frequency range was from 4000 to 550 cm^{-1}, with a resolution of 2 cm^{-1} and 50 scans.

Optical microscopy
Optical microscopy experiments were conducted using an Olympus BX53 with an SC50 camera attached and a Leica DMI 3000B Fluorescence Optical microscope equipped with a Leica DFC7000 T CCD camera. Dark field and fluorescence experiments were conducted using standard filters within each system.

Confocal Laser Scanning Fluorescence Microscopy (CLSFM)
CLSFM characterization was conducted using a Leica SP5-II confocal laser scanning microscope attached to a Leica DMI 6000 inverted epifluorescence microscope. A lens 5x HCX PL Fluotar was used for long working distances.

Scanning Electron Microscopy (SEM) and Energy Dispersive X-ray Spectroscopy (EDS)
The specimen or samples were placed on aluminum specimen stubs with a conductive carbon sticky tab, then sputter-coated with silver (15 nm thick). The samples were then imaged using a JEOL JSM-IT300 at an acceleration voltage of 15 kV and High Current mode for general images and an acceleration voltage of 5 kV in standard current mode for higher resolution images.

For the EDX characterization, an Oxford Instrument X-Max 80 energy dispersive spectrometer was attached to the SEM that was used, with a voltage of acceleration of 30 kV.

Fibre X-ray diffraction
These experiments were done using Rigaku rotating anode (Cu Ka) with Saturn CCD detector with exposure times of 30–60 s and specimen to detector distance of 50- or 100-mm. Reflections were measured using CLEARER.

Macroscopic fibres were used, wherein these refer to either natural fibres or freshly spun biomimetic fibres (within 10 min of fabrication). Briefly, about 1 cm long fibre bundles were mounted on glass capillary tubes using epoxy-based glue and then mounted directly onto a goniometer head for alignment. Alignment was ensured by monitoring a microscope camera focused on the beam path, and alignment was adjusted for the nominal 0 and 90 ° orientations. Spectra were acquired at 50 and 100 mm of distance at 0 and 90° orientations, for 30 and 60 s, respectively.

Wilhelmy plate interfacial analysis
Experiments were conducted using a Force Tensiometer (Krüss K100) at room temperature and a flame-treated platinun Wilhelmy plate. The γ was measured over time to allow for interface equilibration. Each measurement was stopped automatically after the standard deviation of the last 5 points (recorded at 10 s intervals) was <0.01 mN m-1.

Pulling force measurements
Pulling forces were measured using an analytical microbalance. Briefly, droplets of silk solution were deposited on a petri dish on the scale and the instrument was zeroed before pulling the fibres and waiting for steady state (little to no variation on the measured weight was observed, as determined by variations lower than 10%). Apparent measured mass was then annotated and experiment was stopped and fibre broken. Before and after spinning apparent masses were recorded, although no variation was observed. Forces were estimated by calculating the relative force equivalent to measured mass by multiplying it by acceleration of gravity. At least 5 experiments were conducted for each reported pulling speed and values are presented as mean with their respective standard error (1.5x).

Dynamic microindentation
The elastic properties of the protein film at the water–air interface were measured via dynamic microindentation using an FT-MTA03 Micromechanical Testing And Assembly System (FemtoTools AG). Briefly, a standard indentation probe approached the film under microscopic observation at a step size of 5 μm until proximity was observed, but there was no evidence of contact. After this step, the step size was reduced to 1 μm, and the probe was displaced until contact was observed, at which point the probe was moved up by 0.5 μm. The probe then oscillated in a frequency range from 0.1 to 10 Hz and with an amplitude of 1 μm, obtaining the measurements of the elastic (k') and viscous (k") components of the stiffness directly from the instrument without further processing.

Single fibre tensile testing
Single fibres were collected on laser cut cardboard frames with inner window dimension of 20×10 mm along the longest axis by using double-sided tape. Biomimetic single fibres were produced by pulling fibres at the given pulling speeds, waiting for steady state of the system, stopping and then collecting from the filament connecting the droplet and the collector. Fibre diameters were measured by optical microscopy (Leica DFC7000 T) by taking three random measurements of each individual fibre and averaging them, average of each individual fibre was used for their individual tensile data calculations. Tensile testing was done using an Autograph universal tester (Shimadzu, Japan) equipped with a 5 N load cell and subjected to drawing speed of 2 mm/min (10%/min) until fibre break was observed. The reported properties are those of the fibres after storage over 3 months, at ambient temperature, humidity

and pressure. No obvious differences were noted when testing fibres over the entire range of storage. Data was calculated as the engineering stress and strain; force divided by cross-sectional area and displacement divided by fibre length, assumed to be 20 mm, respectively. At least three fibres were used for each pulling speed and reported values correspond to the mean accompanied by the 1.5× standard error.

Fibre composites
Magnetic fibres
Doping NLSF Feedstocks. For the bottom-up functionalization of the biomimetic self-assembly process: 1 mL of NLSF and the desired dopant were made in a desired ratio (e.g. 0.8 mL NLSF and 0.2 mL of 2 mg/ml magnetite nanocrystals).

Synthesis of Magnetite Nanocrystals. 100 ml of ultrapure water was degassed and put under a nitrogen atmosphere; it was heated to 90 °C and stirred vigorously. $FeCl_2 \cdot 4H_2O$ (1.5 g, 7.5 mmol) and $FeCl_3$ (3.0 g, 18.5 mmol) were added to the water under a positive nitrogen gas flow to yield a red/brown solution. Upon complete dissolution, 10 mL of 25 wt% NH_4OH was added gradually with a syringe. This caused the solution to precipitate and turn black. The solution was left to react further for 30 min. The resultant solution was cooled, and the magnetite was isolated through magnetic decantation. The crystals were washed with deionized water several times to remove any remaining chloride ions. The crystals were dried in vacuum oven at 80 °C for 24 h.

E. coli living fibres. BL21(DE3) cells were obtained from the group of Prof. Imre Berger, and the emerald plasmid (Emerald is a version of GFP) was kindly donated by a member within the group. Briefly, standard chemically competent BL21 cells were incubated for 10 min with 200 ng of plasmid before subjecting them to 45 s at 42 C followed by 2 min at 4 C (water/ice), before reconstituting using room temperature Luria broth (LB) and culturing in suspension for 2 h before plating in standard LB-agar supplemented with antibiotic (ampicillin). A primary culture was then made by inoculating 5 ml of LB supplemented with antibiotic with single colonies taken from the LB-gar plate and cultured overnight. In the first instance, primary culture was used to produce fibres by centrifuging the cell suspension at 2000 RCF and resuspending them in autoclaved phosphate saline buffer (PBS). Briefly, primary culture in autoclaved PBS was mixed with silk solution in a 1:10 to 1:500 ratio before readily pulling fibres out of the droplets and culturing these in LB supplemented with antibiotic and 0.5 mM isopropyl β-d-1-thiogalactopyranoside (IPTG) overnight. The following day, fibres were briefly washed with PBS and fixed with 10% formaldehyde for 15 min, washed again in PBS and stored in PBS before observing. In the second instance, a secondary culture was used, where 100 mL of LB with antibiotic were inoculated with 1 mL of primary culture, cultured under shaking until optical density reached 0.6 (absorbance at 600 nm), supplemented with 0.5 mM IPTG and cultured for 2 h before centrifuging the cells and transferring to PBS, to proceed with the method as in the first instance and fixing the silk-cell composite immediately after production.

Data availability
All data are available in the main text or the supplementary materials. Raw data and relevant materials are available upon reasonable request.

References
1. Omenetto, F. G. & Kaplan, D. L. New opportunities for an ancient material. *Sci. (80-.)* **329**, 528–531 (2010).
2. Wen, K. et al. Jellyfish-inspired artificial spider silk for luminous surgical sutures. *Adv. Mater.* **36**, 2314158 (2024).
3. He, W. et al. A protein-like nanogel for spinning hierarchically structured artificial spider silk. *Adv. Mater.* **34**, 2201843 (2022).
4. Walker, A. A., Holland, C. & Sutherland, T. D. More than one way to spin a crystallite: multiple trajectories through liquid crystallinity to solid silk. *Proc. Biol. Sci.* **282**, 20150259 (2015).
5. Sparkes, J. & Holland, C. The energy requirements for flow-induced solidification of silk. *Macromol. Biosci.* **19**, 1800229 (2019).
6. Moreno-Tortolero, R. O. et al. Molecular organization of fibroin heavy chain and mechanism of fibre formation in Bombyx mori. *Commun. Biol.* **7**, 786 (2024).
7. Sparkes, J. & Holland, C. Analysis of the pressure requirements for silk spinning reveals a pultrusion dominated process. *Nat. Commun.* **8**, 594 (2017).
8. Wang, X. et al. Modeling the 3-dimensional structure of the silkworm's spinning apparatus in silk production. *Acta Biomater.* **174**, 217–227 (2024).
9. Shao, Z. & Vollrath, F. Surprising strength of silkworm silk. *Nature* **418**, 741–741 (2002).
10. Moreno-Tortolero, R. O. et al. Silk Road Revealed: Mechanism of silk fibre formation in Bombyx mori. *bioRxiv* 2023.06.02.543394 https://doi.org/10.1101/2023.06.02.543394 (2023).
11. Ling, S. et al. Polymorphic regenerated silk fibers assembled through bioinspired spinning. *Nat. Commun.* **8**, 1387 (2017).
12. Yan, J., Zhou, G., Knight, D. P., Shao, Z. & Chen, X. Wet-spinning of regenerated silk fiber from aqueous silk fibroin solution: Discussion of spinning parameters. *Biomacromolecules* **11**, 1–5 (2010).
13. Koeppel, A. & Holland, C. Progress and trends in artificial silk spinning: a systematic review. *ACS Biomater. Sci. Eng.* **3**, 226–237 (2017).
14. Qiu, W. & Liu, X. Y. Recent progress of applying mesoscopic functionalization engineering principles to spin advanced regenerated silk fibroin fibers. *Adv. Fiber Mater.* **4**, 390–403 (2022).
15. Lu, H. et al. Intelligent perceptual textiles based on ionic-conductive and strong silk fibers. *Nat. Commun.* **15**, 1–9 (2024).
16. Mu, X., Amouzandeh, R., Vogts, H., Luallen, E. & Arzani, M. A brief review on the mechanisms and approaches of silk spinning-inspired biofabrication. *Front. Bioeng. Biotechnol.* **11**, (2023).
17. Qiao, X., Miller, R., Schneck, E. & Sun, K. Foaming properties and the dynamics of adsorption and surface rheology of silk fibroin at the air/water interface. *Colloids Surfaces A Physicochem. Eng. Asp.* 124553 https://doi.org/10.1016/j.colsurfa.2020.124553 (2020).
18. Yang, Y. et al. Behavior of silk protein at the air–water interface. *Soft Matter* **8**, 9705–9712 (2012).
19. Kwak, H. W., Ju, J. E., Shin, M., Holland, C. & Lee, K. H. Sericin promotes fibroin silk I stabilization across a phase-separation. *Biomacromolecules* **18**, 2343–2349 (2017).
20. Koeppel, A., Stehling, N., Rodenburg, C. & Holland, C. Spinning beta silks requires both pH activation and extensional stress. *Adv. Funct. Mater.* **31**, 2103295 (2021).
21. Wan, Q. et al. Mesoscale structure development reveals when a silkworm silk is spun. *Nat. Commun.* **12**, 1–8 (2021).
22. Ling, S., Kaplan, D. L. & Buehler, M. J. Nanofibrils in nature and materials engineering. *Nat. Rev. Mater.* **3**, 1–15 (2018).
23. Li, X. et al. Customized flagelliform spidroins form spider silk-like fibers at pH 8.0 with outstanding tensile strength. *ACS Biomater. Sci. Eng.* **8**, 119–127 (2022).
24. Xu, L., Rainey, J. K., Meng, Q. & Liu, X. Q. Recombinant minimalist spider wrapping silk proteins capable of native-like fiber formation. *PLoS ONE* **7**, e50227 (2012).
25. Bogár, F. et al. On the hofmeister effect: fluctuations at the protein-water interface and the surface tension. *J. Phys. Chem. B* **118**, 8496–8504 (2014).
26. Hao, Z. et al. New insight into the mechanism of in vivo fibroin self-assembly and secretion in the silkworm, Bombyx mori. *Int. J. Biol. Macromol.* **169**, 473–479 (2021).

27. Kronqvist, N. et al. Sequential pH-driven dimerization and stabilization of the N-terminal domain enables rapid spider silk formation. *Nat. Commun.* **5**, 3254 (2014).

28. Zhao, Z., Zhang, H., Lam, J. W. Y. & Tang, B. Z. Aggregation-induced emission: new vistas at the aggregate level. *Angew. Chem. Int. Ed.* **59**, 9888–9907 (2020).

29. Dicko, C., Kenney, J. M. & Vollrath, F. β-silks: enhancing and controlling aggregation. *Adv. Protein Chem.* **73**, 17–53 (2006).

30. Wang, Q. et al. Observations of 3 nm silk nanofibrils exfoliated from natural silkworm silk fibers. *ACS Mater. Lett.* **2**, 153–160 (2020).

31. Wan, Q. et al. Carbon nanotubes facilitate silk hierarchical assembly by dry drawing. *Small Struct.* **5**, 2300435 (2024).

32. Mortimer, B., Holland, C. & Vollrath, F. Forced reeling of bombyx mori silk: Separating behavior and processing conditions. *Biomacromolecules* **14**, 3653–3659 (2013).

33. Mortimer, B., Guan, J., Holland, C., Porter, D. & Vollrath, F. Linking naturally and unnaturally spun silks through the forced reeling of Bombyx mori. *Acta Biomater.* **11**, 247–255 (2015).

34. Lu, H. et al. Highly strong and tough silk by feeding silkworms with rare earth ion-modified diets. *Sci. Bull.* **68**, 2973–2981 (2023).

35. Khurana, R. & Fink, A. L. Do parallel β-helix proteins have a unique fourier transform infrared spectrum? *Biophys. J.* **78**, 994–1000 (2000).

36. Valluzzi, R. & Jin, H.-J. X-ray evidence for a "super"-secondary structure in silk fibers. *Biomacromolecules* **5**, 696–703 (2004).

37. Kratky, O., Schauenstein, E. & Sekora, A. An unstable lattice in silk fibroin. *Nature* **165**, 319–320 (1950).

38. Holland, C., Terry, A. E., Porter, D. & Vollrath, F. Natural and unnatural silks. *Polym. (Guildf.).* **48**, 3388–3392 (2007).

39. Chai, S. et al. Progress in research and application of modified silk fibroin fibers. *Adv. Mater. Technol.* **9**, 2301659 (2024).

40. Wang, J. T. et al. Directly obtaining pristine magnetic silk fibers from silkworm. *Int. J. Biol. Macromol.* **63**, 205–209 (2014).

41. Baeshen, M. N. et al. Production of Biopharmaceuticals in E. *coli: Curr. Scenar. Future Perspect. J. Microbiol. Biotechnol.* **25**, 953–962 (2015).

Author contributions

Conceptualisation: R.O.M.T., S.A.D., L.S., C.H., N.S., R.W. Methodology: R.O.M.T., S.A.D., C.H., L.S. Investigation: R.O.M.T., L.S., J.M., E.W., F.G. Visualisation: R.O.M.T. Funding acquisition: S.A.D., N.S., R.W., R.O.M.T. Project administration: R.O.M.T., S.A.D. Supervision: S.A.D., N.S., R.W. Resources: N.S., R.W., R.O.M.T. Writing – original draft: R.O.M.T., S.A.D. Writing – review & editing: R.O.M.T., N.S., R.W., L.S., C.H., S.A.D.

Competing interests

The authors declare no competing interests.

Additional information

Supplementary information The online version contains supplementary material available at https://doi.org/10.1038/s43246-024-00722-x.

Correspondence and requests for materials should be addressed to Rafael O. Moreno-Tortolero or Sean A. Davis.

Peer review information *Communications materials* thanks the anonymous reviewers for their contribution to the peer review of this work. Primary Handling Editors: Steven Caliari and Jet-Sing Lee. A peer review file is available.

Reprints and permissions information is available at http://www.nature.com/reprints

Publisher's note Springer Nature remains neutral with regard to jurisdictional claims in published maps and institutional affiliations.